Supporting Information

# Fast and sensitive detection of paramagnetic species using coupled charge and spin dynamics in strongly fluorescent nanodiamonds

*F. Gorrini[1]*, R. Giri[1], C. E. Avalos[2], S. Tambalo[1], S. Mannucci[3], L. Basso[1,4], N. Bazzanella[4], C. Dorigoni[1], M. Cazzanelli[1,4], P. Marzola[5], A. Miotello[4] and A. Bifone[1,6]*

[1] Center for Neuroscience and Cognitive Systems, Istituto Italiano di Tecnologia, Corso Bettini 31, 38068 Rovereto, Trento, Italy

[2] Institut des Sciences et Ingénierie Chimiques, Ecole Polytechnique Fédérale de Lausanne (EPFL), Batochime, CH-1015 Lausanne, Switzerland

[3] Department of Neuroscience, Biomedicine and Movement Sciences, University of Verona, Strada Le Grazie 8, 37134, Verona, Italy

[4] Department of Physics, University of Trento, 38123, via Sommarive 14, Povo, Trento, Italy

[5] Department of Computer Science, University of Verona, Strada Le Grazie 15, 37134 Verona, Italy

[6] Department of Molecular Biotechnology and Health Sciences, University of Torino, Italy

*Corresponding Author

E-mail: federico.gorrini@iit.it

## Characteristics of the three NDs types and estimate of dephasing time

The three types of NDs used in this study are indicated in Table S1. The reported average diameters is an estimate, as the NDs have irregular shapes. Diameters measured by scanning electron microscopy (SEM) and dynamic light scattering (DLS) were provided by Bikanta. SEM experiments were also performed in house for further characterization. $T_2^*$ was estimated from both the full-width-half-maximum (FWHM) of optically detected magnetic resonance (ODMR) and from the free induction decay (FID). In the first procedure, the inhomogeneous broadening $\gamma_{in}$ of ODMR signal was measured at various microwaves power intensities. Then $T_2^*$ was calculated according to the relation $T_2^* = {}^1/(\pi\gamma_{in}^0)$, where $\gamma_{in}^0$ is the extrapolated $\gamma_{in}$ at zero microwaves field[1,2]. The second procedure relied on measuring FID of a spin ensemble through Ramsey interferometry. The system was initially prepared in the state $|0\rangle$ and then flipped into the superposition $\frac{1}{\sqrt{2}}(|0\rangle + |-1\rangle)$ with a $\frac{\pi}{2}$ microwave pulse. The FID of the spin ensemble was measured optically and the decay profile was fitted with a single exponential to extract $T_2^*$. The two estimates are in good agreement and return a short value of $\approx 70$ ns, as expected for high-density NV centers.

| ND Type | Diameter (SEM) (*from Bikanta*) [nm] | Diameter (DLS) (*from Bikanta*) [nm] | Coating | $T_2^*$ (ODMR FWHM) [ns] | $T_2^*$ (FID) [ns] |
|---|---|---|---|---|---|
| U40 | 42 ± 16 | 107 ± 0.8 | None | 50 ± 1 | -- |
| U100 | 120 ± 37 | 188 ± 7 | None | 70 ± 2 | -- |
| SC100 | 120 ± 37 core<br>9 ± 2 shell | -- | Silica | 70 ± 1 | 78 ± 6 |

**Table S1.** Size of the NDs, measured by SEM and DLS, functionalization of the surface and $T_2^*$ estimated from the inhomogeneous broadening of the ODMR and from Ramsey interferometry.

## Repolarization dynamics

In this paragraph, we want to show that long lasers pulses, up to 50 µs, do not repolarize the ensemble of NV centers in U100 NDs, in line with previous observations[3]. The adopted pulse sequence is shown in Figure S1. An initializing 532 nm laser pulse of 500 µs and 2 mW of power polarizes the NV ensemble into the $|0\rangle$ state. The $|-1\rangle$ state was optionally populated with the application of a microwave $\pi$ pulse. We determined $\pi = 160$ ns from Rabi oscillations between the states $|0\rangle$ and $|-1\rangle$, at earth's magnetic field. The photon counter gate was opened for 300 ns after a variable $\tau_l$ time from the switching on of the readout pulse. Figure S1 shows the FL intensity

of the $|0\rangle$ and $|-1\rangle$ states (black and red curve, respectively), after $\tau_l$. The repolarization of the $|-1\rangle$ state due to the readout pulse is evident as its FL converges toward the $|0\rangle$ state FL, but only for tens of microseconds long laser readouts. One can see that repolarization (related to the difference of the curves) is negligible after $1-5$ μs of illumination time and is moderate even after tens of microseconds ( $\approx 40\%$ of the NVs reinitialized after 50 μs). This justifies the choice of $1-5$ μs of readout time in most of the experiments and 50 μs when ultrafast single-point acquisition schemes are demanded.

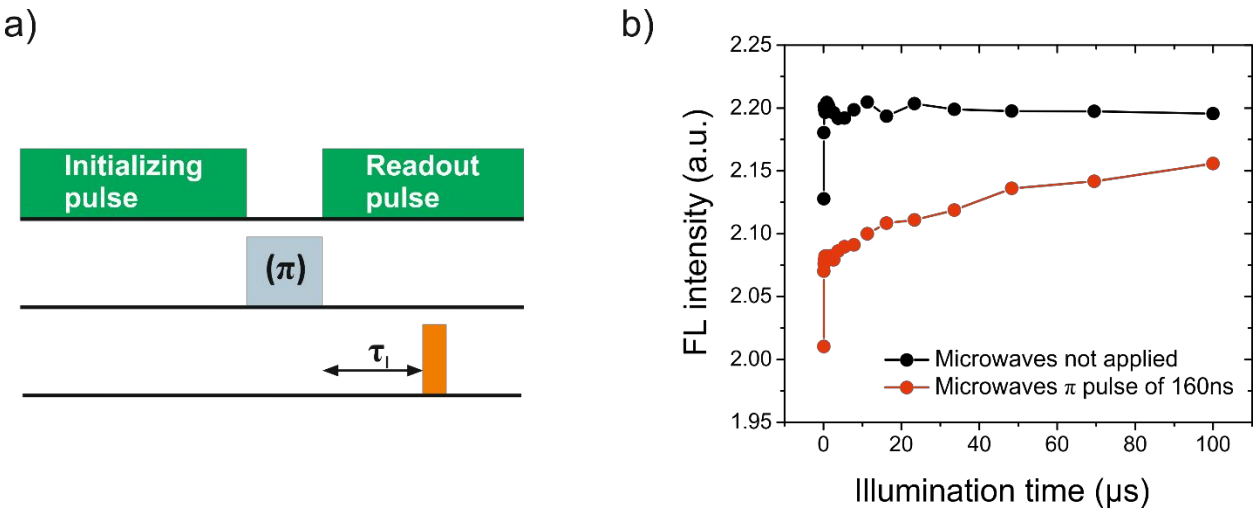


**Figure S1.** Spin repolarization induced by the readout pulse. (a) The sequence used to determine the repolarization time. After the initialization pulse and an optional microwave $\pi$ pulse, the gate is opened for 300 ns, after a variable $\tau_l$ time from the switching on of the readout pulse. (b) Effect of the readout pulse on the system initially in the $|0\rangle$ state (black curve) and in the $|-1\rangle$ state (red curve). In the time interval under consideration the readout pulse does not repolarize considerably the system.

**Population after the initialization pulse**

We can describe the relaxation of an ensemble of NV centers, all in the same conditions, with a four-level scheme with transition rates as indicated in Figure S2. The three lowest levels represent the states $m_s = -1, 0, +1$ of the ground state. The fourth "metastable" level represents the excited state, intermediate singlet states and defects state that can temporarily capture photoexcited electrons from $NV^-$. The normalized populations of each level are thus indicated with $n_0$, $n_{-1}$, $n_{+1}$ and $n_m$. The laser excites the system at a rate proportional to its intensity, $I\sigma$. From the metastable state, the system relaxes to the ground state with rates $k$ (to $m_s = 0$) and $k'$ (to $m_s = \pm 1$ ). Since the metastable level contains the excited states, the conduction band and intermediate singlet states, $I\sigma$ accounts for both excitation and ionization. Further, $k$ and $k'$ should describe radiative as well as non-radiative decays, such as the spin-dependent coupling with the singlet state

(a mechanism known as intersystem crossing, ISC) and recharge. For this reason, $k \neq k'$. After the initialization pulse, the populations of the three levels with $m_s = -1,0,+1$ tend to their equilibrium value at a rate $\gamma$. Solving the rate Equation system gives three exponentials with characteristic times $T_1 = (3\gamma)^{-1}$, $T_r = (k + 2k')^{-1}$ and $T_{mix}^{\pm 1} = (\gamma)^{-1}$. $T_1$ is the longitudinal relaxation time, $T_r$ is the recharge time and $T_{mix}^{\pm 1}$ governs a net transfer of population between $m_s = \pm 1$. We assume that $n_{-1} = n_{+1}$, and $T_{mix}^{\pm 1}$ does not play a role. Populations evolve in time according to the relations:

$$\begin{cases} n_0(t) = \frac{1}{3} + \left(n_0(0) - \frac{1}{3} + \frac{k-\gamma}{k+2k'-3\gamma} n_m(0)\right) e^{-\frac{t}{T_1}} - \frac{k-\gamma}{k+2k'-3\gamma} n_m(0) e^{-\frac{t}{T_r}} \\ n_{\pm 1}(t) = \frac{1}{3} - \frac{1}{2}\left(n_0(0) - \frac{1}{3} + \frac{k-\gamma}{k+2k'-3\gamma} n_m(0)\right) e^{-\frac{t}{T_1}} - \frac{k'-\gamma}{k+2k'-3\gamma} n_m(0) e^{-\frac{t}{T_r}} \\ n_m(t) = n_m(0) e^{-\frac{t}{T_r}} \end{cases} \#(S1)$$

The total fluorescence (FL) intensity, however, depends not only on the populations but also on the different probability of undergoing radiative/non-radiative transitions for $m_s = 0$ and $m_s = \pm 1$. Because of ISC, the FL intensity of the level $m_s = 0$, $l_o$, is larger than $l_1$, the FL of the levels $m_s = \pm 1$. We set $l_1 = q l_0$ and $k' = qk$, with $q \approx 0.7$, similarly to Ref[4]. The overall FL intensity is then

$$I(t) = I_0\left(1 + \beta e^{-\frac{t}{T_1}} - \alpha e^{-\frac{t}{T_r}}\right) \#(S2)$$

with two pre-exponential coefficients related to initial populations according to the relations

$$\begin{cases} \alpha = \frac{2q(1+2q)T_r - 3(1+2q^2)T_1}{(1+2q)^2(T_r - T_1)} n_m(0) \\ \beta = \frac{3(1-q)}{1+2q}\left(n_0(0) - \frac{1}{3} + \frac{(1+2q)T_r - 3T_1}{3(1+2q)(T_r - T_1)} n_m(0)\right) \end{cases} \#(S3)$$

Let's notice that Equation S2 describes the FL profile of an ensemble of NV centers all in the same condition, i.e. with identical $k$, $k'$ and $\gamma$ for all the NVs. We will see in the next paragraph that the magnetic noise experienced by the NVs depend on their distance from the NDs surface. To accommodate the resulting distribution in $T_1$, we introduced stretched exponentials (Equation 1 of the main article).

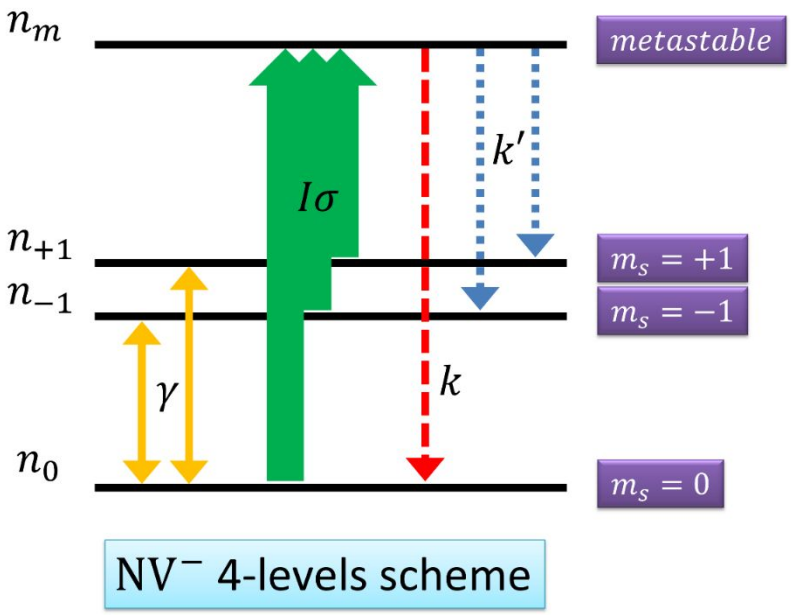


**Figure S2.** 4-level scheme describing the mechanisms of polarization and ionization. At equilibrium, with the laser off, the population of an NV ensemble is equally distributed between the $|0\rangle$ and $|\pm 1\rangle$ states. When the laser is on, the population is pumped into a "metastable" state $|m\rangle$ at a rate $I\sigma$. $|m\rangle$ represents a collection of states (excited states, conduction band, singlet dark states), so $I\sigma$ accounts for both excitation and ionization. From $|m\rangle$ the system can relax to the $|0\rangle$ and $|\pm 1\rangle$ states with decay rates $k$ and $k'$, respectively. Populations in the ground state triplet relax by direct transitions between the $|0\rangle$ and $|\pm 1\rangle$ states (at a rate $\gamma$).

Two things should be remarked about Equations S3. First, both $\alpha$ and $\beta$ depend on $N_{Gd}/N_{NDs}$ and $\beta$, in particular, changes by ≈ 60% in the explored range of deposited gadoteridol (Figure S3). In fact, even if $T_r$ can be fixed to a common value of ≈ 3 ms, $T_1$ does depend on the amount of Gd and, in turn, also $\alpha$ and $\beta$. This observation justifies treating $\alpha$ as a free parameter when fitting experimental curves, differently from $T_r$ and the stretching factor $m$, that are assumed constant. Hence, both charge and spin dynamics contribute to the variation of the FL signal with $N_{Gd}/N_{NDs}$. Second, it is possible to extract the population of the levels right after the laser initialization, at $t = 0$, from $\alpha$ and $\beta$. Reversing Equation S3 we obtain:

$$\begin{cases} n_m(0) = \dfrac{(1+2q)^2(T_r - T_1)}{2q(1+2q)T_r - 3(1+2q^2)T_1}\alpha \\ n_0(0) = \dfrac{1+2q}{3(1-q)}\beta + \dfrac{1}{3} - \dfrac{(1+2q)T_r - 3T_1}{3(1+2q)(T_r - T_1)}n_m(0) \\ n_{\pm 1}(0) = \dfrac{1 - n_0(0) - n_m(0)}{2} \end{cases} \#(S4)$$

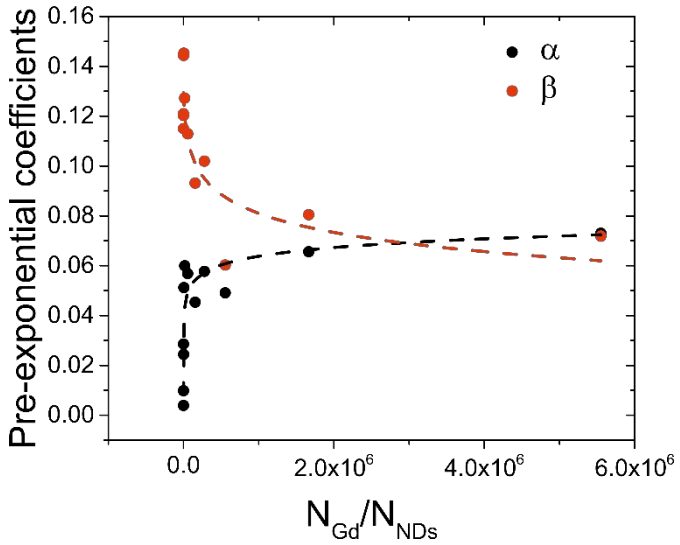


**Figure 3.** Variation of the pre-exponential coefficients $\alpha$ and $\beta$ with $^{N_{Gd}}/_{N_{NDs}}$. The dashed curves are guides for the eye.

Populations as a function of $n_{Gd}$ are plotted in Figure S4. Below the value $^{N_{Gd}}/_{N_{NDs}} = 1000$, $n_0$ and $n_{\pm}$ saturate, while $n_m$ cannot be determined because the recharge component in the FL spectrum is completely overcome by spin relaxation. At higher concentrations, the degree of polarization decreases, and the difference between $n_0$ and $n_{\pm 1}$ is reduced. This is in good qualitative agreement with the observed reduction in the ODMR contrast. The population $n_m$ does not change substantially in the considered range of $n_{Gd}$.

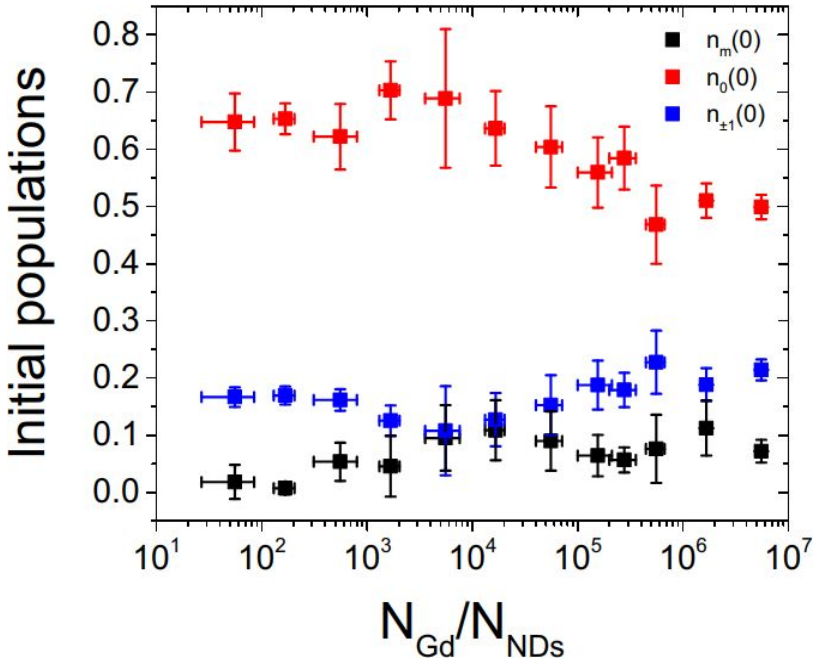


**Figure S4.** Initial populations, after the initialization pulse. $n_0$ indicates the polarized fraction of the NVs, while $n_{-1} = n_{+1}$ represent the population in the $|\pm 1\rangle$ states of the ground state triplet. $n_m$ indicates the fraction of NVs that have been ionized. We see that $n_m$ does not change substantially with the amount of deposited Gd, while the polarization decreases at high $n_{Gd}$. This is consistent with the observed reduction in the ODMR contrast. Error bars on the x-axis come from the dilution procedure; error bars on the y-axis come from those of the relaxation times, $T_1$ and $T_r$.

## Computation of $T_1$ of NV ensemble in presence of gadoteridol

The additional relaxation term in Equation 2 of the main article contains two quantities that depend on the amount of gadoteridol: the variance of the transverse magnetic field $\langle B_\perp^2 \rangle$ and the rate of Gd fluctuations $f_{Gd}$., The magnetic dipolar field generated by a single Gd ion at a position $\mathbf{R'}_i$ from the NV center is

$$\mathbf{B}_i = \frac{\mu_0 \gamma_e \hbar}{4\pi R'^3_i}\left[\mathbf{S}_i - \frac{3(\mathbf{S}_i \cdot \mathbf{R'}_i)\mathbf{R'}_i}{R'^2_i}\right].\#(S5)$$

The variance $\langle B^2_{\perp,i} \rangle$ is $\langle B_i^2 - B^2_{z,i} \rangle$. The following theoretical model is derived as in Ref[4]. We take the average of $\mathbf{B}_i$ over the possible values of $\mathbf{S}_i$ by taking the trace with a purely mixed state, with density matrix $\rho = \frac{1}{2S+1}\mathbb{1}_{2S+1}$, where $\mathbb{1}_{2S+1}$ is the identity matrix of size $2S+1$. Then

$$\langle B_{\perp,i}^2 \rangle = \mathrm{Tr}\{\rho(B_i^2 - B_{z,i}^2)\} = \left(\frac{\mu_0 \gamma_e \hbar}{4\pi}\right)^2 S(S+1)\frac{5 - 3\cos^2\Theta'}{3R_i'^6} \#(S6)$$

where $\Theta'$ is the angle between $\mathbf{R}'_i$ and the quantization axis of the NV center, taken along the $z$-axis. The origin of the coordinate axis is at the center of the ND. A generic NV center has spherical coordinates $(r,\vartheta,\varphi)$ and a generic Gd ion has spherical coordinates $(R,\Theta,\Phi)$. The noise variance $\langle B_{\perp,i}^2 \rangle$ depends also on the coordinates of the NV center inside the ND, through the relations $R_i'^2 = (\mathbf{R} - \mathbf{r})^2$ and $R'\cos\Theta' = R\cos\Theta - r\cos\vartheta$.

The mean noise variance amplitude on a particular NV center takes the contribution of all the spins surrounding each ND, so it depends on the number $N_{Gd}/N_{NDs}$. To simplify the calculation, it is helpful to use momentarily a continuous density of Gd ions per unit volume $n_{Gd}$ (the conversion between the two quantities being straightforward). This means to replace a sum with an integral of Equation S6:

$$\langle B_\perp^2 \rangle = \sum_i \langle B_{\perp,i}^2 \rangle \approx \left(\frac{\mu_0 \gamma_e \hbar}{4\pi}\right)^2 S(S+1) n_{Gd} \int_{R_{ND}}^{+\infty} dR R^2 \int_0^\pi d\Theta \sin\Theta \int_0^{2\pi} d\Phi \frac{5 - 3\cos^2\Theta'}{3R'^6} \#(S7)$$

The result is independent on the azimuthal angle $\varphi$ and depends only on the polar angle $\vartheta$ and on the reduced radius $\xi = r/R_{ND}$:

$$\langle B_\perp^2 \rangle(\xi,\vartheta) = C_1 \left[\frac{3 - \cos^2\vartheta}{(1-\xi^2)^3} + \frac{1 - 3\cos^2\vartheta}{8\xi^2}\left(\mathrm{atanh}\,(\xi) - \frac{\xi(1+\xi^2)}{(1-\xi^2)^2}\right)\right] \#(S8)$$

where $C_1 = \frac{2\pi}{3R_{ND}^3}\left(\frac{\mu_0 \gamma_e \hbar}{4\pi}\right)^2 S(S+1) n_{Gd}$. The value of $\xi$ runs up to a maximum value of $\approx 0.95$ for the U100 NDs and $\approx 0.9$ for the U40 NDs, so it assumes that NV centers too close to the surface (within 2-3 nm) are not stable in the negative form[5].

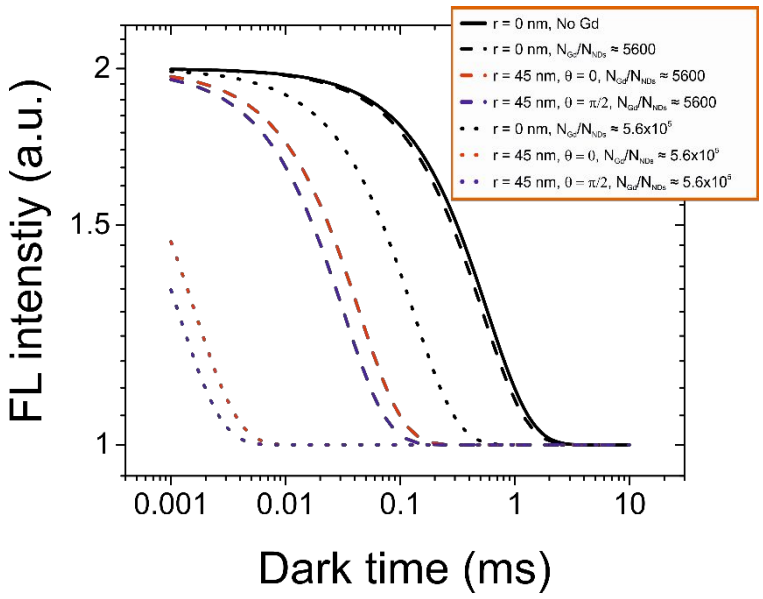


**Figure S5.** Simulation of the spin-related decay of FL for a single NV center inside a nanodiamond. The symmetry axis of the NV is along the z-axis. Black curves: FL decay profile for an NV at the center of the ND, with no Gd (solid line), with $^{N_{Gd}}/_{N_{NDs}} = 5600$ (dashed line), and with $^{N_{Gd}}/_{N_{NDs}} = 5.6 \times 10^5$ (dotted line). Red curves: luminescence decay for an NV at 45 nm from the center, along the z-axis ($\vartheta = 0$), with $^{N_{Gd}}/_{N_{NDs}} = 5600$ and with $^{N_{Gd}}/_{N_{NDs}} = 5.6 \times 10^5$ of Gd (dashed and dotted lines, respectively). Blue curve: same luminescence decay profile for an NV at 45 nm from the center, on the equatorial plane ( $\vartheta = 90°$), with $^{N_{Gd}}/_{N_{NDs}} = 5600$ and with $^{N_{Gd}}/_{N_{NDs}} = 5.6 \times 10^5$ of Gd (dashed and dotted lines, respectively). The red and blue solid lines coincide with the black one: without Gd, all the NV centers have the same $T_1$, since no relaxation mechanism other than Gd-paramagnetic noise has been considered here (no cross-relaxation and surface charges effect).

The rate of Gd fluctuations $f_{Gd}$ includes a constant vibrational term[6] $f_{vib} \approx 1$ GHz and a dipolar term $f_{dip}$ that depends on the amount of Gd ions. The dipolar interaction between a Gd spin $\mathbf{S}_i$ with all the other spins $\mathbf{S}_j$ of the bath gives an estimate of $f_{dip}$. Explicitly: $hf_{dip} = \sqrt{\sum_{j \neq i} \langle H_{ij}^2 \rangle}$, where $H_{ij}$ is the interaction between two magnetic dipoles

$$H_{ij} = \frac{\mu_0 \gamma_e^2 \hbar^2}{4\pi R_{ij}^3} \left[ \mathbf{S}_i \cdot \mathbf{S}_j - \frac{3(\mathbf{S}_i \cdot \mathbf{R_{ij}})(\mathbf{S}_j \cdot \mathbf{R_{ij}})}{R_{ij}^2} \right] \#(S9)$$

where $\mathbf{R_{ij}}$ is the vector connecting the two spins. The quantity $\langle H_{ij}^2 \rangle$ is equal to $\mathrm{Tr}\{\rho H_{ij}^2\}$, with the two-spins density matrix $\rho = \frac{1}{(2S+1)^2} \mathbb{1}_{2S+1} \otimes \mathbb{1}_{2S+1}$. So

$$\langle H_{ij}^2 \rangle = \left(\frac{\mu_0 \gamma_e^2 \hbar^2}{4\pi}\right)^2 \frac{2S^2(S+1)^2}{3R_{ij}^6} \#(S10)$$

and once again, the summation over j can be replaced by an integral:

$$\sum_{j \neq i} \langle H_{ij}^2 \rangle \approx \left(\frac{\mu_0 \gamma_e^2 \hbar^2}{4\pi}\right)^2 \frac{2S^2(S+1)^2}{3} n_{Gd} \int_{R_{min}}^{R_{max}} dR_{ij} 4\pi R_{ij}^2 \frac{1}{R_{ij}^6} \#(S11)$$

If $R_{min}$ is about the size of a gadoteridol molecule, $d_{Gd}$, and $R_{max} \gg R_{min}$, then

$$f_{dip} \approx \frac{\mu_0 \gamma_e^2 \hbar}{6\sqrt{2\pi^3}} S(S+1) \sqrt{\frac{n_{Gd}}{d_{Gd}^3}} \#(S12)$$

Finally, the reduction of $T_1$ due to Gd spins, compared to its value without Gd $T_1^0$, can be described by

$$\frac{1}{T_1}(\xi,\vartheta) = \frac{1}{T_1^0} + k_1(\xi,\vartheta) \frac{n_{Gd}\left(\sqrt{n_{Gd}} + k_2\right)}{n_{Gd} + 2k_2\sqrt{n_{Gd}} + k_3} \#(S13)$$

with $k_2 = 0.8423$ nm$^{-3/2}$, $k_3 = 6.5532$ nm$^{-3}$ and

$$k_1(\xi,\vartheta) = 1.1347 \cdot 10^{-5} \text{ GHz nm}^{\frac{3}{2}} \cdot \left[\frac{3 - \cos^2\vartheta}{(1-\xi^2)^3} + \frac{1 - 3\cos^2\vartheta}{8\xi^2}\left(\text{atanh}\,(\xi) - \frac{\xi(1+\xi^2)}{(1-\xi^2)^2}\right)\right] .\#(S14)$$

A few examples of FL decay with Gd are shown in Figure S5: let's notice that the usual dependence over $N_{Gd}/N_{NDs}$ is recovered.

However, the FL comes from many NV centers in different positions inside each ND. This means integrating numerically the Equation S13 over $r$, $\vartheta$ and $\xi$, to obtain a time-dependent FL curve:

$$I\left(t, N_{Gd}/N_{NDs}\right) = \int_0^{r_{max}} dr r^2 \int_0^{\pi} d\vartheta \sin\vartheta \int_0^{2\pi} d\varphi e^{-\frac{t}{T_1(\xi,\vartheta)}} \sim I_0 e^{-\left(\frac{t}{T_1}\right)^n} \#(S15)$$

where $I_0$ is just a coefficient for the luminescence, and the values of the effective longitudinal relaxation time $T_1$ and the stretching coefficient $n$ are obtained by fitting $I\left(t, N_{Gd}/N_{NDs}\right)$. Values of $n$ for the U100 NDs obtained with this procedure are shown in Figure S6. Even if we do not consider any explicit model for recharge, we expect that the contribution to the growing component of the FL should be described by a stretched exponential, following a similar procedure that led to Equation S15.

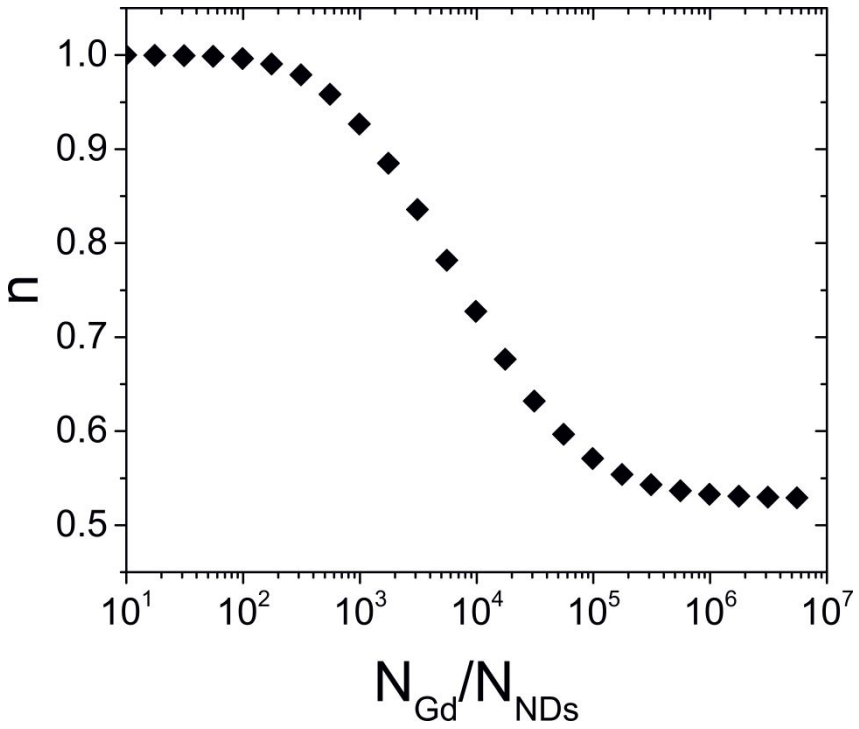


**Figure S6.** Values of $n$ obtained by fitting with Equation S15 the numerically computed FL profile.

The NDs/Gd mixture is a heterogeneous system, where Gd can both decorate the surface of NDs and also fill the empty spaces between packed NDs. To simplify the derivation of $\langle B^2_{\perp,i} \rangle$ we considered a single ND, immersed in pure gadoteridol, with no other NDs in the surroundings. Analogously, in the derivation of $f_{dip}$ we considered a homogeneous system of pure gadoteridol, with no NDs at all. This heterogeneity of the system means that the effective amount of Gd interacting with NDs is lower than the one reported. From the best fit of the theoretical curve of Figure 2a, we empirically found that only $15 - 30\%$ of gadoteridol interacts efficiently with NDs.

**Estimate of sensitivity and acquisition time**

Finally, we empirically estimate the sensitivity of NV ensemble to variations in the amount of deposited gadoteridol, from a state that has already been characterized through its FL. To this end, we must compare the variation in the number of photons detected at a certain time, $\delta\mathcal{N}_{ph}(t)$, with the level of photon shot noise, $\delta\mathcal{N}_{noise}(t)$. The number of photons detected at a fixed time $t$ after $N_{iter}$ iterations is

$$\mathcal{N}_{ph}(t) \approx \mathcal{R}\tau_{ro}N_{iter}\left(1+\beta e^{-\left(\frac{t}{T_1}\right)^n}-\alpha e^{-\left(\frac{t}{T_r}\right)^m}\right)\#(S16)$$

where $\mathcal{R}$ is the detector counting rate (number of detected photons per unit time) and $\tau_{ro}$ the integration time (the length of the readout pulse). The photon shot noise scales as the square root of the signal:

$$\delta\mathcal{N}_{noise}(t) \approx \sqrt{\mathcal{R}\tau_{ro}N_{iter}\left(1+\beta e^{-\left(\frac{t}{T_1}\right)^n}-\alpha e^{-\left(\frac{t}{T_r}\right)^m}\right)}\#(S17)$$

On the other side, if the number of gadoteridol molecules changes with time by a small amount $\delta\left(N_{Gd}/N_{NDs}\right)$ this will result in a variation in the number of photons detected

$$\delta\mathcal{N}_{ph}(t) \approx \frac{d\mathcal{N}_{ph}(t)}{d\left(N_{Gd}/N_{NDs}\right)}\delta\left(N_{Gd}/N_{NDs}\right)\#(S18)$$

where the derivative in Equation S18 accounts for the variation of all the parameters described in Equation S16, nominally $T_1$, $\alpha$, $\beta$ and also $n$ (which ranges continuously from 0.5 to 1), with respect to $N_{Gd}/N_{NDs}$. Let's clarify that these variations were calculated empirically from the fit of experimental data. Again, we assume that the recharge mechanism, and therefore the parameters $T_r$ and $m$, is independent of the magnetic noise. The contrast to noise ratio can be written as:

$$CNR\left(t,N_{Gd}/N_{NDs}\right) = \frac{\delta\mathcal{N}_{ph}}{\delta\mathcal{N}_{noise}}(t) = \mathcal{C}F(t)\delta\left(N_{Gd}/N_{NDs}\right)\#(S19)$$

where $\mathcal{C} = \sqrt{\mathcal{R}\tau_{ro}N_{iter}}$ is a number that depends only on detection conditions and $F(t)$ is a function of the spin- and charge-related parameters, their derivatives, and time. We see that CNR benefits from the high density of NV centers. In fact, the presence of a recharge mechanism contributes positively to the variation $\delta\mathcal{N}_{ph}$. Further, the high NV density allows high photon counting rates (up to $\sim 10^7 s^{-1}$) and long readout pulses (up to tens of microseconds), as described above, and consequently leads to a large $\mathcal{C}$ coefficient.

Numerically, we find that $CNR_{max}\left(N_{Gd}/N_{NDs}\right)$, the maximum of Equation S19, depends on $N_{Gd}/N_{NDs}$ and is located at $t_{max}\left(N_{Gd}/N_{NDs}\right)$, varying a lot between $\approx 0.003T_1$ and $\approx T_1$. This result is different from the simple exponential case without charge dynamics, where the maximum is always located at $t_{max} = \frac{T_1}{2}$, independently of $N_{Gd}/N_{NDs}$. The value of $CNR_{max}\left(N_{Gd}/N_{NDs}\right)$ can be arbitrarily increased by a sufficiently large number of experimental iterations $N_{iter}$ (via the

coefficient $\mathcal{C}$). Thus, in a single-point detection scheme, a particular value of $CNR_{max}\left(N_{Gd}/N_{NDs}\right)$ is attained after $N_{iter}$, or equivalently after a total experimental time of

$$\Delta t_{exp}\left(N_{Gd}/N_{NDs}\right) = N_{iter}\left(\tau_{in} + \tau_{ro} + t_{max}\left(N_{Gd}/N_{NDs}\right)\right) = \frac{\mathcal{C}^2}{\mathcal{R}\tau_{ro}}\left(\tau_{in} + \tau_{ro} + t_{max}\left(N_{Gd}/N_{NDs}\right)\right) \quad \#(S20)$$

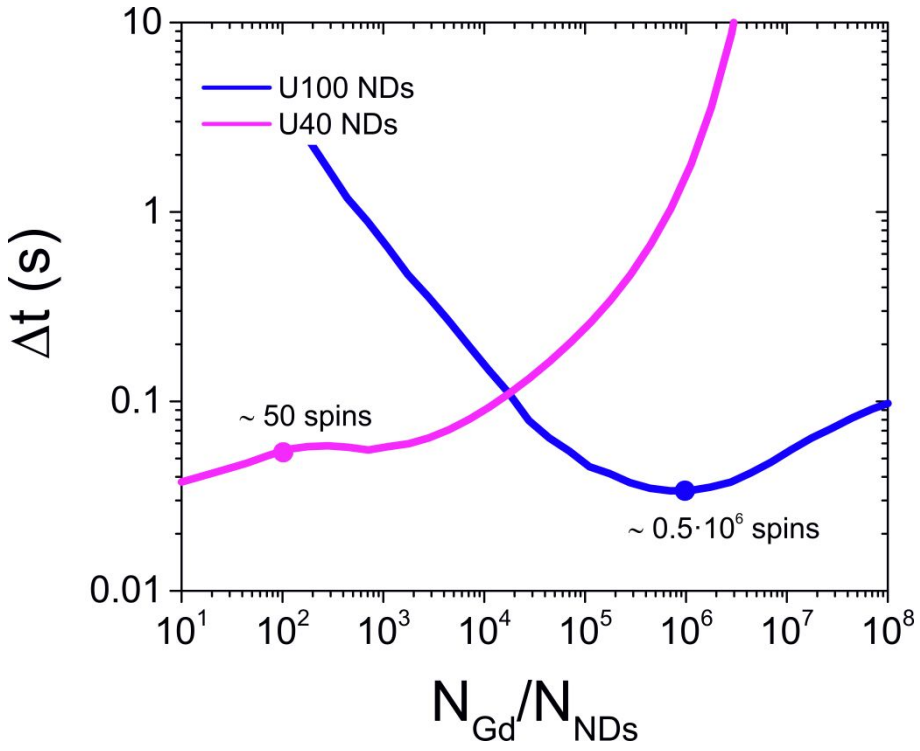


**Figure S7.** Acquisition time needed to sense variation of 50% of the $N_{Gd}/N_{NDs}$ for U40 NDs (pink curve) and U100 NDs (blue curve). The U100 NDs can sense a 50% variation over $10^6$ spins in ≈ 35 ms, while the U40 NDs can detect an increment of 50 Gd spins over 100 in less than 60 ms.

Using Equations S19 and S20 and choosing $CNR_{max} = 3$, which is sufficient to detect a variation in the signal, it is possible to relate $\Delta t_{exp}$ to $\delta\left(N_{Gd}/N_{NDs}\right)$:

$$\Delta t_{exp}\left(N_{Gd}/N_{NDs}\right) = \left(\frac{3}{F(t_{max})\delta\left(N_{Gd}/N_{NDs}\right)}\right)^2 \frac{\left(\tau_{in} + \tau_{ro} + t_{max}\left(N_{Gd}/N_{NDs}\right)\right)}{\mathcal{R}\tau_{ro}} \quad \#(S21)$$

Once again, a large ensemble of NV centers means a large value of the product $\mathcal{R}\tau_{ro}$, resulting in short acquisition times. A plot of $\Delta t_{exp}\left(N_{Gd}/N_{NDs}\right)$ necessary to sense a 50% variation in $N_{Gd}/N_{NDs}$ is shown in Figure S7, for the U100 and U40 NDs. The quantity $F(t_{max})$ depends

crucially on the NDs size, so different NDs display ultrashort acquisition times in specific ranges of $N_{Gd}/N_{NDs}$. For example, the U100 NDs can detect a 50% change over $10^6$spins in 35 ms, while, for the U40 NDs, $\Delta t_{exp}$ is shorter than 60 ms for $N_{Gd}/N_{NDs} < 1000$.

**Results of the single-point measurement in a liquid droplet**

We tested the fast single-point measurement in a system where a 20 µL of gadoteridol at 0.5 M are deposited on a spot of dry U40 NDs. In this way, the NDs are immersed in a liquid environment. We recorded the FL level at 1 µs and at 1 ms and took the ratio (Figure S8a). The contrast is then defined as

$$C = \left(1 - \frac{I(1\text{ ms})}{I(1\text{ µs})}\right) \#(S22)$$

As the droplet evaporates the concentration increases with time until the value of 1.32 M where precipitation takes place. The fast single-point measurement can detect the instantaneous value of concentration by looking at the contrast (Figure S8b).

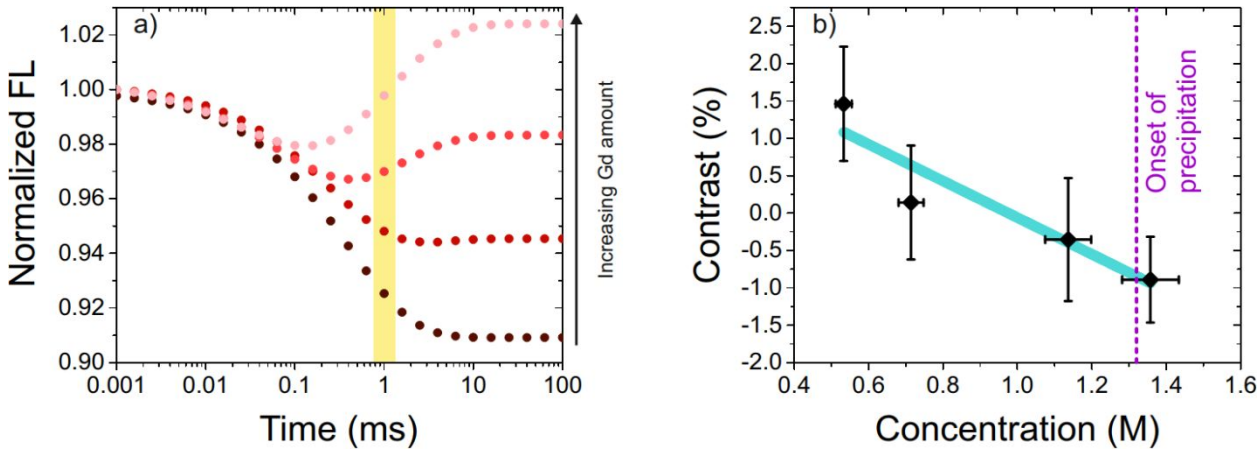


**Figure S8.** Single point test experiment in a droplet. The droplet of gadoteridol has a starting concentration of 0.5 M, but upon evaporation the concentration increases. This affects the FL shape (theoretical simulations in (a)), with a second component arising and a change in the contrast, as defined by Equation S16. The reference point to calculate the contrast has been taken at 1 ms (yellow stripe). (b) The contrast can then be used to distinguish between the concentrations of 0.5 M and 1.32 M, at the onset of precipitation.

# References


1 Abragam, A. *The Principles of Nuclear Magnetism*. (Clarendon Press, 1970).

2 Ishikawa, T. *et al.* Optical and spin coherence properties of nitrogen-vacancy centers placed in a 100 nm thick isotopically purified diamond layer. *Nano letters* **12**, 2083-2087 (2012).
3 Giri, R. *et al.* Coupled charge and spin dynamics in high-density ensembles of nitrogen-vacancy centers in diamond. *Physical Review B* **98**, doi:10.1103/PhysRevB.98.045401 (2018).
4 Tetienne, J. P. *et al.* Spin relaxometry of single nitrogen-vacancy defects in diamond nanocrystals for magnetic noise sensing. *Physical Review B* **87**, 235436 (2013).
5 Bluvstein, D., Zhang, Z. & Jayich, A. C. B. Identifying and mitigating charge instabilities in shallow diamond nitrogen-vacancy centers. *Physical review letters* **122**, 076101 (2019).
6 Kaufmann, S. *et al.* Detection of atomic spin labels in a lipid bilayer using a single-spin nanodiamond probe. *Proceedings of the National Academy of Sciences* **110**, 10894-10898, doi:10.1073/pnas.1300640110 (2013).